RESEARCH ARTICLE
SOLID EARTH: GEODESY AND GRAVITY

Earth and Planetary Physics
6: 96–107, 2022
doi: 10.26464/epp2022009

Spatial distribution characteristics and mechanism of nonhydrological time-variable gravity in China continent

Yue Shen, QiuYu Wang, WeiLong Rao, and WenKe Sun*

University of Chinese Academy of Sciences, Beijing 100049, China

Key Points:

- Using multi-source hydrological data to construct a new more comprehensive hydrological model in China.
- The spatial distribution of the transfer signals due to nonhydrological mass in China continent was obtained by subtracting the combined hydrological model from the GRACE time-variable gravity field.
- Further studied and discussed the spatial distribution characteristics and mechanism of the nonhydrological mass transfer signals of China continent.

Citation: Shen, Y., Wang, Q. Y., Rao, W. L., and Sun, W. K. (2022). Spatial distribution characteristics and mechanism of nonhydrological time-variable gravity in China continent. *Earth Planet. Phys.*, *6*(1), 96–107. http://doi.org/10.26464/epp2022009

Abstract: The purpose of this study is to explore nonhydrological mass transfer in China continent. For this purpose, gravity recovery and climate experiment (GRACE) data were obtained to study the spatial distribution of time variant gravity signals in China continent. Then, from auxiliary hydrological data processed according to the current hydrological model, a new more comprehensive hydrological model of China continent was constructed. Finally, the time variant signals of this new hydrological model were removed from the time variant gravity field computed from GRACE data, thus obtaining a description of the nonhydrological mass transfer of China continent. The physical sources and mechanisms of the resulting mass transfer are then discussed. The improved, more realistic, hydrological model used here was created by selecting the hydrological components with the best correlations in existing hydrological models, by use of correlation calculation, analysis, and comparison. This improved model includes water in soils and deeper strata, in the vegetation canopy, in lakes, snow, and glaciers, and in other water components (mainly reservoir storage, swamps, and rivers). The spatial distribution of the transfer signals due to nonhydrological mass in China continent was obtained by subtracting the combined hydrological model from the GRACE time-variable gravity field. The results show that the nonhydrological signals in China continent collected in GRACE data were mainly positive signals, and were distributed in the Bohai Rim and the northern and eastern parts of the Tibetan Plateau. The above nonhydrological mass transfer signals have been studied further and are discussed. The results show that the nonhydrological mass migration signals in the Bohai Rim region originate primarily from sea level change and marine sediment accumulation. The mass accumulation from Indian plate collision in the Tibetan Plateau appears to be the main reason for the increase in the residual gravity field in that region.

Keywords: GRACE; hydrological model; time-variable gravity signal; nonhydrological signal

1. Introduction

Global mass transfer is often accompanied by a change in the Earth's gravity field, which can be observed by modern geodetic observation technologies. Time-variable data describing this gravity field can be used in scientific analysis of surface mass transfer around the world. Specifically, the Earth's spheres and their interactions are accompanied by mass migration which can be detected in time-variable gravity fields. For example, the global hydrosphere, cryosphere, and lithosphere are changing at all times, accompanied by hydrological mass changes such as the exchange of hydrological components (including soil moisture, runoff, groundwater and snow cover), sea level change, polar ice mass balance, and sea ice change. Simultaneously, the mass changes of solid earth include seismic deformation (Xing LL et al., 2021; Dong J et al., 2021), volcanic activity, GIA (Glacial Isostatic Adjustment) effects, and tectonic movement. These mass transfers are important scientific issues considered by scientists.

Effective research on global mass transfer benefits from the successful launch of gravity satellites, especially the GRACE (Gravity Recovery and Climate Experiment) satellite in 2003. GRACE satellite data provide an unprecedented global-scale high-precision time-variable gravity field (Tapley et al., 2004), which is a revolutionary observation technology to study global surface mass migration (Chen JL, 2019) that has already led to a large amount of scientific research and allowed unprecedented scientific progress. For example, Syed et al. (2008) and Chen JL et al. (2010) used GRACE monthly gravity solution data to study changes in Total

Correspondence to: W. K. Sun, sunw@ucas.ac.cn
Received 11 AUG 2021; Accepted 15 OCT 2021.
Accepted article online 24 DEC 2021.

Water Storage (TWS) globally, and nonseasonal and interannual change characteristics of TWS in the Amazon basin; they found that drastic changes in land water reserves are often accompanied by extreme climate events. Rodell et al. (2009) and Tiwari et al. (2009) studied changes in groundwater storage in India, finding from GRACE data and hydrological models that India has experienced serious groundwater loss. Feng W et al. (2013) used GRACE data to verify changes in groundwater storage in the North China Plain where human activities have caused serious groundwater loss. Yi S and Sun WK (2014) studied the issue of ice and snow melting in the high mountains of Asia, gave a reasonable estimation of the change rate, and found that there was a periodic change of approximately 5 years in the Pamir Plateau. Zhang L et al. (2019) investigated the application of Mascon gravity products on different spatial scales, studying fully and discussing, as an example, the melting of Tianshan snow and ice, and summarized the progress and prospect of GRACE Mascon products and their applications (Zhang L and Sun WK, 2022). Chang L et al. (2019) used Argo and CTD data to estimate the global heat capacity change at sea level caused by deep-sea temperature change below 2000 meters, proposed a new research method to calculate global thermosteric sea level change, and confirmed the global sea level changes obtained from GRACE observational data. Wang QY et al. (2021), based on ICESat-1, 2 and GRACE/GRACE follow-on observation data, calculated a continuous estimation of the mass balance of alpine glaciers in Asia, including interannual and trend changes. Scholars generally believe that gravity signals in the Tibetan Plateau, a research hotspot, are best explained by three physical sources: the first is the negative signal caused by groundwater loss from northern India (Rodell et al., 2009; Tiwari et al., 2009), the second is the signal of glacier mass balance (Matsuo and Heki, 2010; Jacob et al., 2012), and the third is lake storage change (Zhang GQ et al., 2013) and tectonic movement.

Most of the above mentioned studies address changes in global or regional hydrological mass. Few studies have addressed mass transfers of solid earth. The main reason is that the mass change accompanied by changes in the global hydrological system is usually considered to be the main factor in global mass migration, while the change of solid mass accompanied by earth tectonic movement is comparatively small, thus not significant relative to hydrological change. However, researchers have found that surface mass migration changes reflected by GRACE gravity satellites may be affected by nonhydrological signals in addition to hydrological mass changes. For example, in the Tibetan Plateau, as the third pole of the word formed by the collision of the Indian plate and Eurasia, the mass migration caused by tectonic movement can also be observed by GRACE time-variable gravity (Jiao JS et al., 2019; Rao WL and Sun WK, 2021). Tectonic movement includes mainly surface vertical displacement, Moho interface fluctuation, denudation, and sedimentation. It is worth noting that GIA (postglacial isostatic adjustment) is also a part of the change in Earth's solid mass. However, since GIA can be directly predicted or calculated according to the model, it is treated independently and is not considered as the research object of solid mass migration.

As mentioned above, research on mass migration caused by tectonic movement has been insufficient, the primary difficulty having been how to remove surface hydrological signals. Some hydrological models, including the Global Land Data Assimilation System (GLDAS) and WaterGAP Global Hydrologic Model (WGHM), have been developed, yet research has demonstrated great differences among them. Hydrological models need the support and supplementation of precipitation, temperature, and observational data, but the distribution of meteorological observation stations in different regions is not uniform over large areas; data have therefore been insufficient to verify the accuracy of hydrological models. In addition, the water composition in current hydrological models has not been comprehensive, which further calls into doubt their reliability. Building a reasonable hydrological model from existing hydrological models is not only a challenge but also an urgent issue because a reliable hydrological model is crucial to and must be a basis for studying changes in surface mass caused by nonhydrological factors.

Thus we begin by obtaining the time-variable gravity field of China continent from GRACE data. Existing hydrological models and supplementary data were used to build synthetic hydrological models and compute corresponding hydrologic time-variable gravity fields. Finally, the hydrologic gravity field was deducted from the GRACE time variant gravity field to obtain the nonhydrological time-variable gravity field in China continent. The spatial distribution and possible physical mechanisms of nonhydrologic mass changes in China continent are discussed.

2. GRACE Time-Variable Gravity Field in China Continent

In March 2002, GRACE, a gravity satellite with low-satellite tracking technology developed by the National Aeronautics and Space Administration (NASA) and Deutsches Zentrum für Luft- und Raumfahrt (DLR), was successfully launched. GRACE consists of two satellites, GRACE A and GRACE B, approximately 500 kilometers from the ground. Their orbit is approximately circular; the satellites are approximately 220 kilometers apart.

To obtain static and time-variable gravity field information with high precision and high spatial resolution, changes in the distance between the two GRACE satellites is monitored by using Ka-Band microwave Ranging (KBR) between them for low-low (STS-ll) tracking; for high-low (STS-hl) tracking, their positions are compared to the space-bone global positioning system (GPS).

In this study, level-2 RL06 gravity satellite data released by the University of Texas Space Research Center (UT-CSR) was used. The data have a 60-degree regularized spherical harmonic coefficient, the time span is from January 2003 to December 2016, and the spatial resolution is 1° × 1°. The GRACE gravity satellite data used in this study allowed us to deduct the solid tide, ocean tide, polar tide, high-frequency ocean signals, and the nontidal atmospheric signal. The result can thus be expected to reflect the sum of the time-variable gravity signal of the surface mass migration, residual signal, and the observational noise not completely deducted by the model. Due to systematic correlation error between the odd (even) order of GRACE spherical harmonic coefficients, there will be obvious north-south strip error in the data calculation. A Gaussian filter with a smoothing radius of 300 km (Wahr et al., 1998) and decorrelation of P4M6 (Swenson and Wahr, 2006) was used. Considering the impact of glacier isostatic adjustment (GIA) on the surface mass distribution (Sheng YY et al., 2020), the GIA

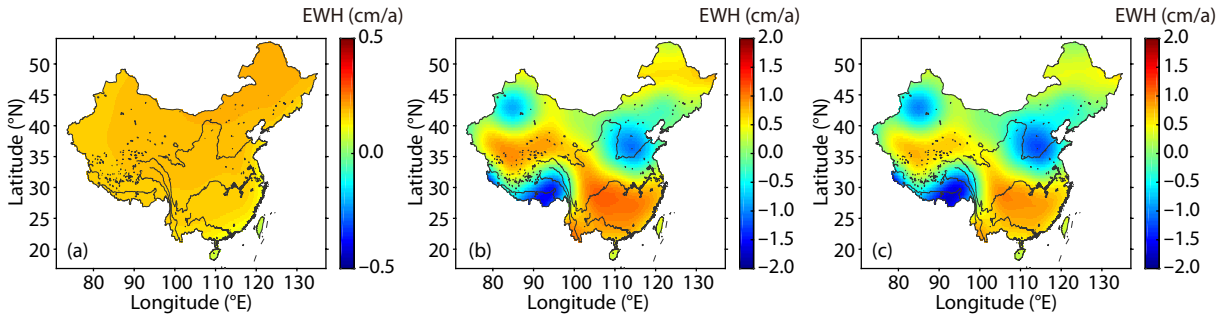

Figure 1. Spatial distribution of GIA gravity change (a), GRACE time-variable gravity signal (b), and corrected GRACE time-variable gravity signal (c) in China continent.

model of Geruo et al. (2013) was adopted in this study (as shown in Figure 1a). In addition, due to the earth's oblateness and geocentric offset, the accuracy of the low-order terms of the GRACE data was poor. The C_{20} and first-order terms were therefore replaced with values measured by satellite laser ranging (SLR) (Cheng and Tapley, 2004); the resulting spatial distribution of GRACE time-variable gravity signals in China continent is plotted in Figure 1b. After deducting the influence of the GIA effect from the revised GRACE time-variable gravity signal (Geruo et al., 2013), the spatial distribution map of the GIA-corrected time-variable gravity signal in China continent was obtained, as drawn in Figure 1c.

The adjusted GRACE time-variable gravity field, illustrated by Figure 1c, shows mass migration in China continent and is the comprehensive embodiment of the total mass change corresponding to various physical factors. In essence, it contains two kinds of mass change information, i.e., hydrologic signals and nonhydrological signals (tectonic signals). Because many researchers have studied the contribution of hydrological signals to the time-variable gravity field, the focus of this study is the nonhydrological signal, i.e., the time-variable gravity field corresponding to tectonic movement.

The relationship among GRACE time-variable gravity (ΔGRACE), hydrological gravity signal (Δhydrology), and nonhydrological signal (Δnonhydrology) can be expressed:

$$\Delta g = \Delta\text{hydrology} + \Delta\text{nonhydrology}, \quad (1)$$

where the symbol Δ represents time-variable gravity. To obtain the time-variable gravity signal generated by a nonhydrological signal, it was necessary to deduct the time-variable gravity signal of a land hydrological signal obtained from a hydrological model and supplementary empirical data. Most researchers (Yi S et al., 2016b; Rao WL and Sun WK, 2021) have considered only the effects of soil water, snow water, glacier, and groundwater components when calculating changes in TWS. Generally, the impact of other water components is relatively small, but that does not mean that they have no impact. In addition, on the Tibetan Plateau, the lake water level has changed significantly in recent years; this phenomenon, too, should be considered a hydrological signal and included in any TWS calculation. Therefore, in our work, the standard components of hydrological signals were supplemented; vegetation canopy water was also considered, in addition to other water component information, dominated by reservoirs, swamps, and rivers. Therefore, the calculation of hydrological variation in this paper adopts Equation (2):

$$\Delta\text{hydrology} = \Delta\text{soil} + \Delta\text{snow} + \Delta\text{groundwater} + \Delta\text{lake} + \Delta\text{glacier} + \Delta\text{vegetation} + \Delta\text{reservoir} + \Delta\text{swamps} + \Delta\text{rivers}. \quad (2)$$

3. Time-variable Gravity Field of Hydrological Signal

Obtaining an accurate time-variable gravity field of hydrological signals is an important premise and foundation for the study of nonhydrological time-variable gravity problems. In this section, building a reasonable hydrological model, especially how to obtain it through different hydrological models according to the composition of hydrological components in Equation (2), is discussed. The GLDAS hydrological model, WGHM hydrological model, and ICESat altimetry satellite data are the primary components used here.

3.1 GLDAS Hydrologic Model

First, the GLDAS hydrological model was used to obtain the TWS change model. The primary components of this hydrological model are soil water change, snow water mass change, and vegetation canopy water change. The GLDAS hydrological model (Global Land Surface Data Assimilation System) was established by the NASA Goddard Flight Center (NASA) and the National Center for Environmental Prediction (NCEP). The model integrates multisource observation data, land surface models, and atmospheric assimilation data and constructs several submodels, such as Noah, CLSM, VIC and Mosaic. The GLDAS hydrological model has been updated to a second version. We selected the GLDAS hydrological model with spatial resolution of 1° × 1° and the Noah, CLSM, VIC, and Mosaic datasets with time resolution of one month.

In the field of hydrology, the GLDAS hydrological model has become the main data source for most researchers (Syed et al., 2008; Moghim, 2020) to obtain information regarding changes in landwater or soil-water reserves. However, the GLDAS hydrological model does not simulate changes in deep groundwater or in surface lakes and reservoirs (Rodell et al., 2004). Therefore, when using the GLDAS hydrological model to calculate changes in TWS, only three components — soil water, vegetation canopy water, and snow water — are usually used. In addition, the data sources and parameter models adopted by the four submodels are different, resulting in significant differences among different submodels, suggesting that none of them can be considered accurate. Given these differences among the Noah, CLSM, VIC, and Mosaic

submodels, this study made an optimal selection of the same three water components — soil water, vegetation canopy water, and snow water — and constructed a combined hydrological model of just these three.

To weaken the influence of differences between the models and to improve the accuracy of the new hydrological model, a correlation analysis was conducted on the three water components of the model; the result gives the spatial distribution of the combined sum of change trends in soil water, snow water, and vegetation canopy water content (Figure 2). To illustrate the differences among the submodels, the time series diagram of the mass change trends of different water components in each submodel was calculated (Figure 3). The results expose great differences among models for all three water components as well as among their partial and total sums.

To analyze quantitatively the differences and correlations between the models, the Pearson statistical correlation coefficient was used in this study ($\rho_{X,Y}$) to measure the correlation between hydrological models, and the calculation principle is shown as:

$$\rho_{X,Y} = \frac{\sum_{i=1}^{n}\left(X_i-\overline{X}\right)\left(Y_i-\overline{Y}\right)}{\sqrt{\sum_{i=1}^{n}\left(X_i-\overline{X}\right)^2}\sqrt{\sum_{i=1}^{n}\left(Y_i-\overline{Y}\right)^2}}, \tag{3}$$

where X_i and Y_i are the measured values of the i-th epoch of the two variables and represent the average values of the two groups, respectively; n is the total number of observations; the value range is [−1, 1], where −1 and 1 represent negative and positive maximum correlation, respectively.

Correlation between two models of the same water component were compared, two groups of models with the highest correlation were selected, and an arithmetic average was made as the optimal data choice for that water component. The correlation results of soil water, snow water equivalence, and vegetation canopy water in the different models (CLSM, Noah, VIC and Mosaic) are shown in Tables 1–3, respectively. The calculation results show that the two groups of models with the best correlation in soil water composition were the Noah and VIC models, the two groups with the best correlation in snow water equivalent data were Noah and CLSM, and the two with the best correlation in vegeta-

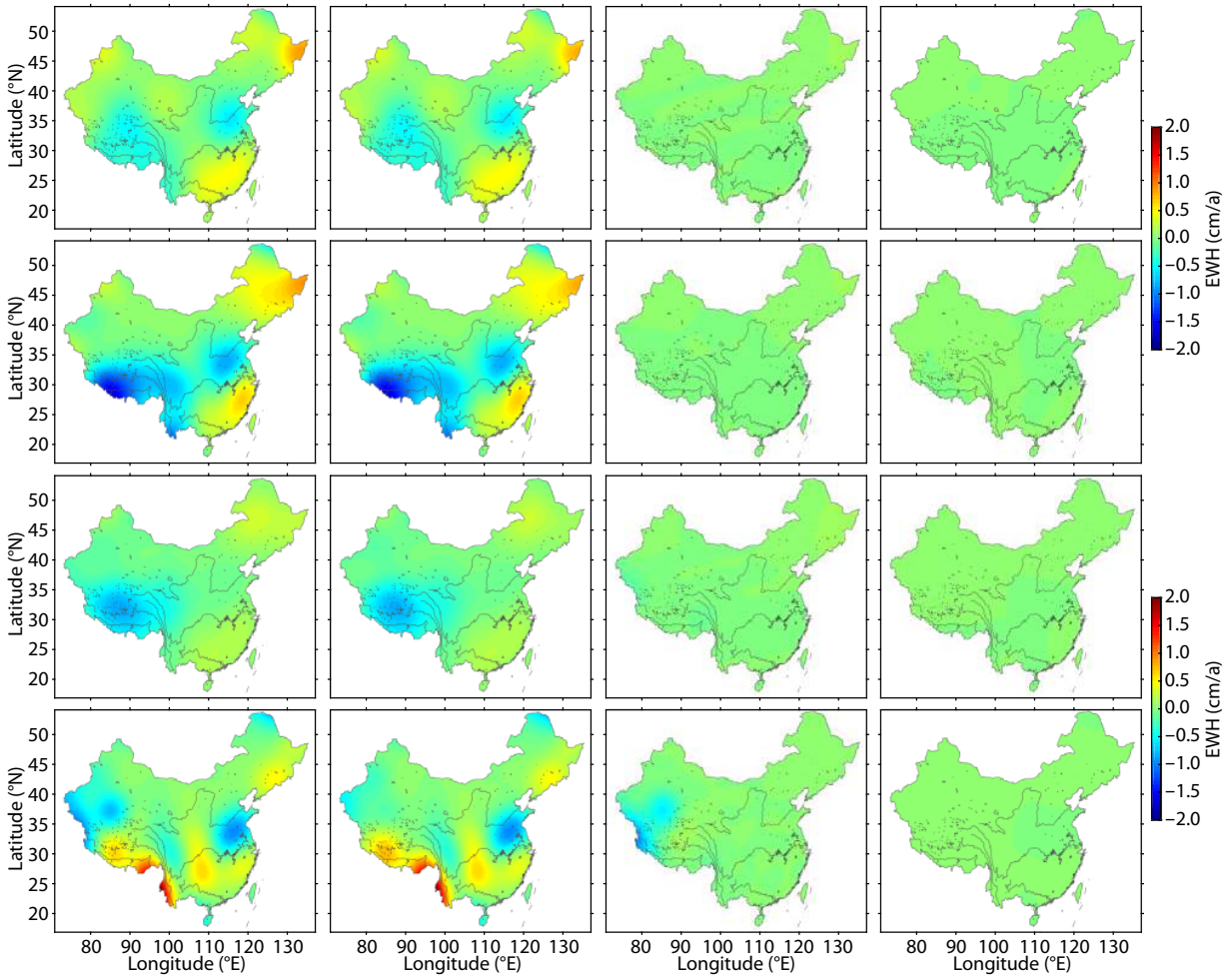

Figure 2. Spatial distribution map of the variation trend of soil water (second column), snow water (third column), vegetation canopy water (fourth column) and the sum of the three (first column) provided by Noah (first row), CLSM (second row), VIC (third row) and Mosaic (fourth row) of the GLDAS hydrological model in China continent.

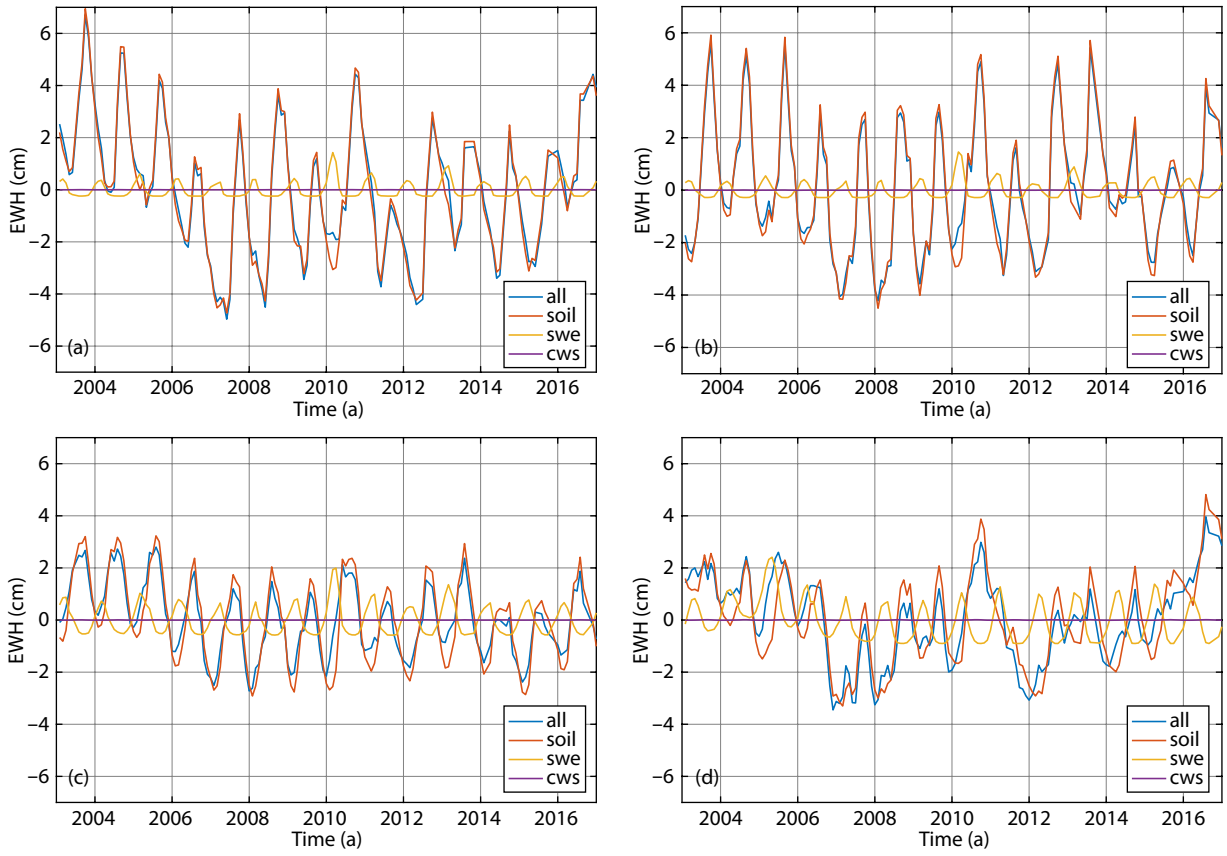

Figure 3. Time series of mass changes of soil water, snow water, vegetation canopy water, and the sum of the four submodels GLDAS CLSM (a), Noah (b), VIC (c) and Mosaic (d) in China continent.

Table 1. Correlation results of soil water components among the Noah, CLSM, VIC and Mosaic submodels.

The correlation	Noah	CLSM	VIC	Mosaic
Noah	1.000	0.786	**0.835**	0.755
CLSM	0.786	1.000	0.564	0.806
VIC	**0.835**	0.564	1.000	0.660
Mosaic	0.755	0.806	0.660	1.000

Table 2. Correlation results of snow water equivalence components among the Noah, CLSM, VIC and Mosaic submodels.

The correlation	Noah	CLSM	VIC	Mosaic
Noah	1.000	**0.970**	0.960	0.571
CLSM	**0.970**	1.000	0.889	0.439
VIC	0.960	0.889	1.000	0.733
Mosaic	0.571	0.439	0.733	1.000

Table 3. Correlation results of vegetation canopy water components among the Noah, CLSM, VIC and Mosaic submodels.

The correlation	Noah	CLSM	VIC	Mosaic
Noah	1.000	0.885	0.920	0.933
CLSM	0.885	1.000	0.972	0.972
VIC	0.920	0.972	1.000	**0.975**
Mosaic	0.933	0.972	**0.975**	1.000

tion canopy water were Mosaic and VIC. Therefore, the soil water components of the Noah and VIC models were calculated and averaged, as were the snow water components of the Noah and CLSM models, and the vegetation canopy water of the Mosaic and VIC models; these averages yield the optimal combination model of soil water, snow water and vegetation canopy water data. Figure 4 shows the spatial distribution of the sum of the above three water components, and their respective hydrological mass change trends of the combined model obtained in this study.

3.2 WGHM Hydrologic Model

The WaterGAP Global Hydrologic Mode (WGHM) is a global water resource analysis and prediction model provided by the University of Frankfurt, Germany. WGHM is composed of a global hydrological model and a large number of water models for irrigation, livestock, thermal power plants, and household life (Alcamo et al., 2003). Different from the GLDAS model, the WGHM model not only calculates the long-term average water resources of each country or watershed but also simulates all components of land water reserves except glaciers, including changes in soil water, runoff, groundwater recharge, surface snow, and surface water reserves (such as vegetation canopy water, rivers, lakes, reservoirs and wetlands). In this study, the groundwater and other water components (mainly reservoir impoundment, swamps, rivers, etc.) datasets of the WGHM hydrological model were adopted, the spatial resolution was 0.5° × 0.5°, and the time resolution was 1 month.

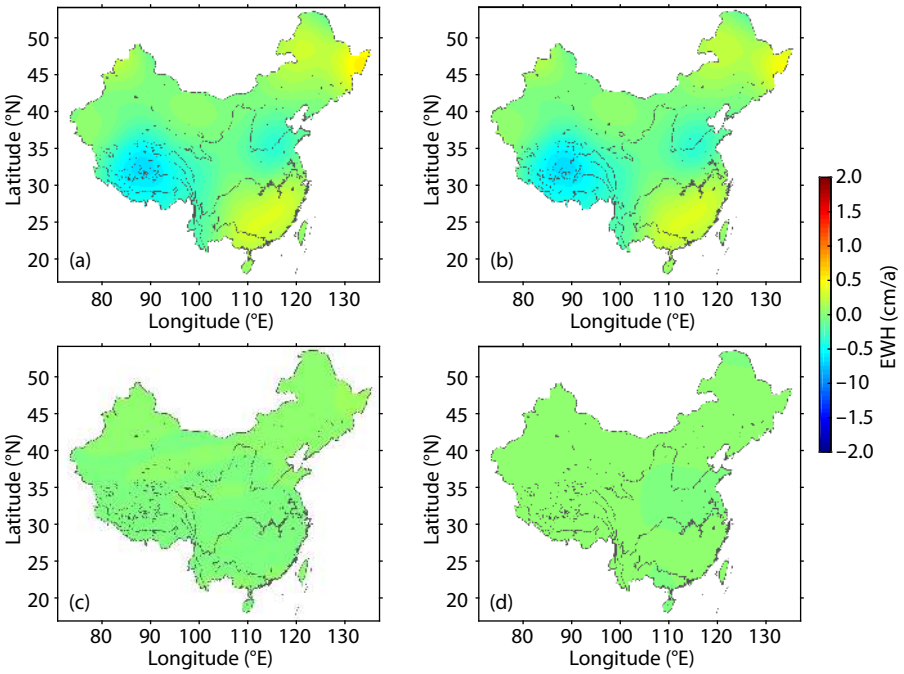

Figure 4. Spatial distribution map of the variation trends of (b) soil water, (c) snow water equivalence, (d) vegetation canopy water and their sum (a) in China continent, obtained from the combined model.

3.3 ICESat Dataset

The Ice, Cloud, and Land Elevation Satellite (ICESat), developed by Texas State University and NASA, is the first laser ranging satellite operating in near polar orbit, with a flight altitude of approximately 600 km and an inclination of 94°. It was successfully launched on January 13, 2001 (https://nsidc.org/data/icesat/). The ICESat satellite is equipped with an Earth science laser altimeter system (GLAS). GLAS includes a laser that can emit short pulses (4 ns) of infrared light to measure surface elevation, and visible green light to measure backscattered aerosols. The primary scientific objective of the ICESat satellite is to measure glacier changes and the heights of clouds and aerosols. It also has a powerful sensor that can measure the elevation of land terrain and surface water. The vertical accuracy of ICESat satellite data can reach the decimeter level in areas with relatively flat terrain, especially in open waters; horizontal data accuracy can reach approximately 5 cm (Duong et al., 2008). In addition, compared with radar satellites, ICESat satellites have smaller sampling spot sizes, so the spatial resolution of sampling data is higher, making it possible to monitor water level changes in lakes with relatively small areas.

To obtain the contribution of lake water and glacier mass to the hydrological model, lake water level change data derived from ICESat observations were selected in this study (Zhang GQ et al., 2019). Considering that glaciers in China are mainly concentrated on the Tibetan Plateau, this study uses ICESat data to estimate the mass change caused by glacier melting in this area (Gardner et al., 2013).

3.4 Combined Hydrological Model

Selection of the main hydrological models and their components was discussed above. In this section, a combined hydrological model based on the above discussion is constructed. The observed data and models used in this study and their sources are summarized in Table 4.

Table 4. Datasets involved in this study and their sources.

Data	Issuing agency
Total mass change	GRACE CSR (2003–2016) (Bettadpur, 2012)
Soil, snow, vegetation canopy waters	GLDAS Noah/CLSM/VIC/Mosaic (Liang X et al., 1994; Koster and Suarez, 1996; Koste et al., 2000r; Beaudoing and Rodell, 2016)
Groundwater	WGHM (2003–2016) (Döll et al., 2003)
Surface water	WGHM (2003–2016) (Döll et al., 2003)
Lake water	ICESat/ICESat2 (Zhang GQ et al., 2019)
Glacier	ICESat (2003–2009) (Gardner et al., 2013)
GIA	Geruo et al. (2013)

Before constructing the combined hydrological model, it was necessary to preprocess the data. The main steps were: 1. within each dataset, to select data from the same time span as GRACE data, 2. to compare other data directly to GRACE results, it was necessary to transform, truncate, filter, and de-smooth the spherical harmonic coefficient of each hydrological model's data, 3. units needed to be unified, by converting the time-variable gravity or hydrological model into an expression of equivalent water height, in units of cm/a.

The process of obtaining soil water, snow water, and vegetation canopy water components is described in Section 3.1. Groundwater, lakes, glacier water, and other water components were provided primarily by the WGHM hydrological model. The results of these water model components are plotted in Figure 5. The

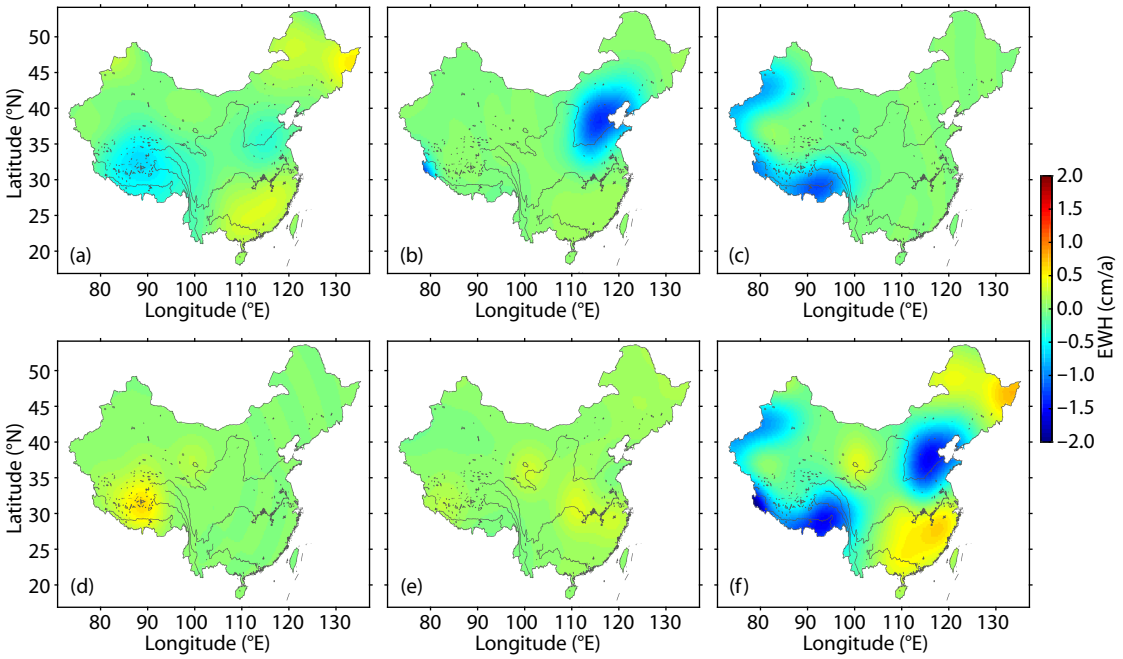

Figure 5. Sum of soil water, snow water, and vegetation canopy water obtained by GLDAS hydrological Model (a), groundwater composition of WGHM hydrological Model (b), glacier mass distribution obtained by ICESat data (c), lake water composition obtained by ICESat/ICESat 2 (d), the spatial distribution of other water components (e) of WGHM hydrological model, and the total hydrological mass change trend (f) after the addition of all water components.

subplots in Figure 5 show the sum of soil water, snow water, and vegetation canopy water obtained by the GLDAS hydrological Model (Figure 5a), groundwater composition provided by the WGHM hydrological Model (Figure 5b), glacier mass change obtained by ICESat data (Figure 5c), lake water information provided by ICESat/ICESat 2 (Figure 5d), and other water components provided by the WGHM hydrological model (reservoir storage, swamp water, spatial distribution of river (Figure 5e), and the total hydrological mass variation trend (Figure 5f) summed by all water components above. Figure 5f is the combined hydrological model obtained in this study, which basically considers all hydrological signals in China continent and can reflect the spatial distribution of the total hydrological mass.

To calculate the uncertainty of the combined hydrological model, least square fitting was used to determine the uncertainty of each individual water component. According to the error analysis, the uncertainty of the combined hydrological model is ±0.22 cm/a.

Figure 5f displays an obvious signal of water loss in the North China Plain, which is consistent with the conclusions of previous research; i.e., it confirms previous evidence that a shortage of water resources in the North China Plain has been caused by artificial exploitation of groundwater in that region (Feng W et al., 2013). In the southern part of the Tibetan Plateau, there is an obvious negative signal, which is explained primarily by the melting of glaciers around the Tibetan Plateau but also reflects negative signal leakage caused by overexploitation of groundwater in India. For South China, there is a positive signal distribution. Chang L and Sun WK (2020) conducted research on this topic and concluded that South China shows a positive signal due to the growth of green plants, increasing vegetation water storage, and the filling of soil water content in recent years.

4. Spatial Distribution Characteristics of Nonhydrological Mass Transfer Signals

The purpose of this study was to identify and study the spatial distribution characteristics of nonhydrological mass transfer signals in China continent. In the second and third sections, the GRACE time-variable gravity field was obtained in China continent (Figure 6a) and compared to the combined hydrological model (Figure 6b). When the water mass calculated in the combined hydrological model is subtracted from the GRACE time-variable gravity field, the remaining signal should be equivalent to the spa-

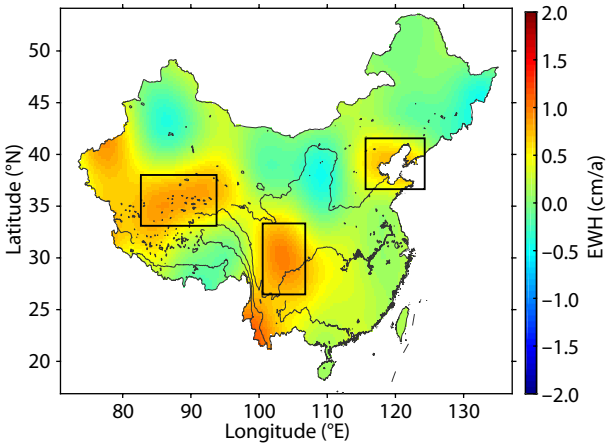

Figure 6. The time-variable map showing the spatial distribution of nonhydrological gravity signals is obtained by subtracting hydrological signals from the GRACE time-variable gravity field.

tial distribution of the nonhydrological mass transfer. If all the mass migration in China continent were caused by hydrological changes, then the residual signal should be zero, confirming that the time-variable fields observed by GRACE were caused exclusively by hydrologic factors. If the residual signal is not zero, however, then the residual signal must reflect mass migration generated by tectonic movement in China continent. The residual signals (nonhydrological information) are plotted in Figure 6c.

Comparing Figures 6a and 6b, we can see that the GRACE time-variable gravity and combined hydrological model results have similar magnitudes and spatial distribution characteristics, indicating that the GRACE data generally reflect the trend and characteristics of hydrological change in China continent. However, careful inspection reveals large differences between the two, which are captured in the remaining (residual) signal (Figure 6c). Figure 6c shows that the residual signals were concentrated primarily in the north of the Tibetan Plateau, the east of the Tibetan Plateau, and the Bohai Rim, as shown in the red box of Figure 6c. The sources and physical mechanisms of these residual signals are discussed below.

4.1 Leakage Effect of Ocean Signal

First, the positive signal observed in the Bohai Sea is considered.

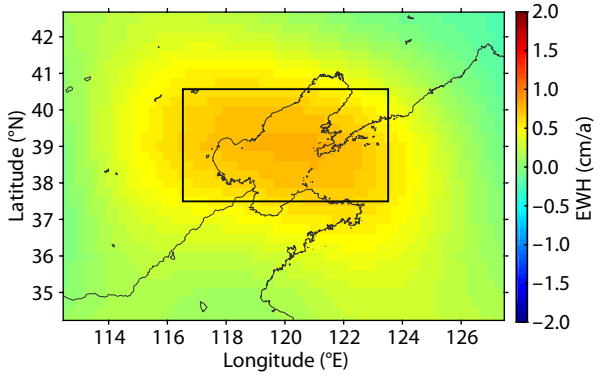

Figure 7. Spatial distribution of nonhydrological mass signals after deducting hydrological signals in the Bohai Sea.

For this purpose, the spatial distribution of mass change after deducting hydrological signals in the Bohai Sea area was supplemented and calculated (red box area in Figure 7). By least squares fitting of the time series of the nonhydrological mass change trend, the mass change trend in this area was calculated to be 0.62 cm/a. But the hydrological model does not include consideration of the impact of sea level changes on surrounding gravity signals, which might be contributing to this rather large residual signal (Figure 6c).

Accordingly, to improve the accuracy of the time-variable gravity information of nonhydrological signals in the Bohai Sea, data from altimetry satellites were used to obtain the leakage signal of sea level change in China's coastal areas. The altimeter data time period and data processing method used were consistent with the GRACE data. The impact of sea level change on the time-variable gravity signal in the Bohai Sea was calculated to be approximately 0.2 cm/a, as shown in Figure 8a. The spatial distribution of nonhydrological signals obtained after deducting this influence of sea level change is shown in Figure 8b. Figure 8b shows that the raw "nonhydrological" mass migration signal in the Bohai Rim region is significantly reduced after removal of the gravitational signal caused by sea level change.

To further refine the residual signal, so that it would still more accurately reflect true nonhydrological mass migration around the Bohai Sea, we considered another possible influencing factor: marine sedimentation. The Bohai Sea is at the mouth of the Yellow River, China's second longest river, which flows mainly through Qinghai, Gansu, Ningxia, Shaanxi, Shanxi, Henan, and Shandong. In these areas, especially through the Loess Plateau where it acquires a large amount of sediment, the Yellow River, as its name implies, is known to have the highest sediment content of all the world's rivers. The deepest point in the Bohai Sea is only 83 m; its average depth is as shallow as 18 m. Therefore, when the Yellow River flows into the Bohai Sea with a large amount of sediment, this sediment will either be precipitated or directly suspended in the water of the Bohai Sea.

To calculate the time-variable gravity signal of sediment brought by the Yellow River into the Bohai Sea, the China River sediment

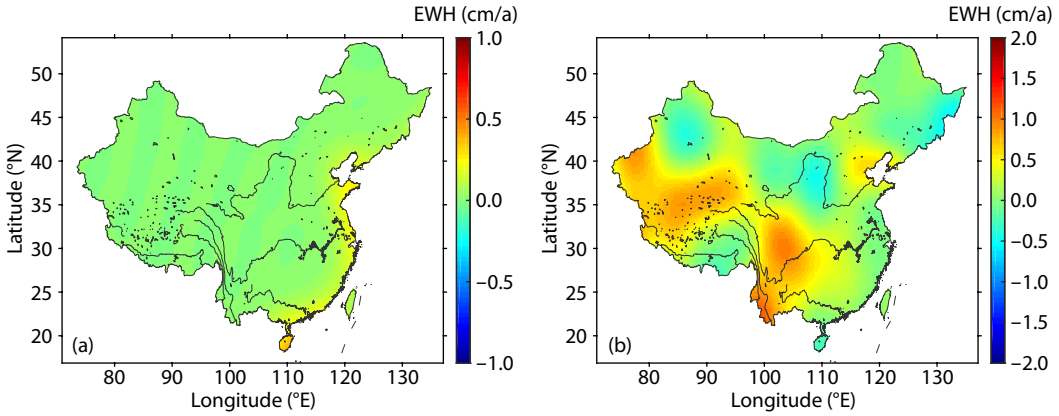

Figure 8. (a) The time-variable gravity signals caused by sea level changes obtained from satellite altimetry data on China's coastal areas and (b) the net spatial distribution of nonhydrological signals after deducting the impact of sea level water mass variations.

bulletin was used to count the annual sediment discharge (unit: 100 million tons) from 2003 to 2016, as measured by the Lijin hydrological control station at the end of the main stream of the Yellow River. The specific data are shown in Table 5.

According to the sediment transport data in Table 5, the average annual sediment transport is 140 million tons. Combined with the area of the Bohai Sea, which is approximately 77284 square kilometers, the effect of marine sediments on the time-variable gravity signal (equivalent water height) calculated in the Bohai Sea was approximately 0.2 cm/a. Similarly, after spherical harmonic expansion, 60th degree truncation, Gaussian smoothing, and decorrelation of sediment data, the spatial distribution map of the trend of sediment mass change in the Bohai Sea area was obtained, as shown in Figure 9a; the time-variable gravity signal after deducting the marine sedimentary signal is shown in Figure 9b. These results further weaken the residual signal around the Bohai Sea; the final net signal is not significantly different from the signals in the north and east of the Tibetan Plateau.

Considering that the uncertainty of the combined hydrological model was ±0.22 cm/a, the positive signal change in the Bohai Sea appears to have been affected primarily by the sediments brought out from the Yellow River, the accumulation in the Bohai Sea accounting for the apparent increased mass. According to the analysis of elevation data, Mu DP et al. (2020) found that the water mass in the Bohai Sea shows an increasing trend, and the calculated increase was approximately 0.44 Gt/a. Chang L and Sun WK (2021) found that the average sea level change trend of the Bohai Sea from 1993 to 2019 was 3.3 ± 0.7 mm/a.

Therefore, the sea level change on signal leakage in China's coastal areas cannot be ignored. However, we conclude that the positive signal of the Bohai Rim region was caused by the deposition of sediments into the sea in the Bohai region.

4.2 Signal Interpretation in the Northern and Eastern Tibetan Plateau

Next, the migration of nonhydrological mass in the Tibetan Plateau is discussed. This area is characterized by complex and diverse geophysical phenomena, such as glacier melting, changes in soil water, lake water, and groundwater caused by climate conditions, and tectonic movement, all of which redistribute mass and contribute to the time-variable gravity field. Figure 6c shows that the nonhydrological signals in the Tibetan Plateau are mainly positive signals, primarily distributed in the north and east of the Tibetan Plateau. Generally, these positive signals reflect primarily the tectonic movement of the Tibetan Plateau.

In addition to the GIA effect, the gravity signals in the Tibetan Plateau may also be caused by crustal flow movement, surface erosion, crustal uplift, and other factors. Yi S et al. (2016a) calculated the movement of crustal flow in the eastern Tibetan Plateau according to the observation data of GRACE time-variable gravity and GPS displacement fields and found that the change in gravity was approximately 0.32 μGal/a. Rao WL and Sun WK (2021) analyzed the complex gravity signals in the Tibetan Plateau; they suggested that the mass signals in the region were affected not only by hydrology but also by changes in the Moho surface, crustal movement, and surface erosion. They found that the crustal uplift rate in the Tibetan Plateau was approximately 0.12 ± 0.03 cm/a, that the Moho uplift rate was approximately 0.18 ± 0.22 cm/a, and that the denudation and sediment accumulation rate was approximately −0.07 ± 0.02 cm/a. Therefore, the net change rate caused by tectonic movement factors was approximately 0.23 ± 0.27 cm/a.

Sedimentology research results are used to discuss this issue. Based on crustal volume balance theory, Westaway (1995) gave numerical estimations of deposition on the Tibetan Plateau dur-

Table 5. Annual sediment discharge (unit: 100 million tons) from 2003 to 2016 obtained by the Lijin hydrological control station at the end of the main stream of the Yellow River.

Time	2003	2004	2005	2006	2007	2008	2009	2010	2011	2012	2013	2014	2015	2016
Discharge	3.69	2.58	1.91	1.49	1.47	0.77	0.56	1.67	0.93	1.83	1.73	0.30	0.31	0.11

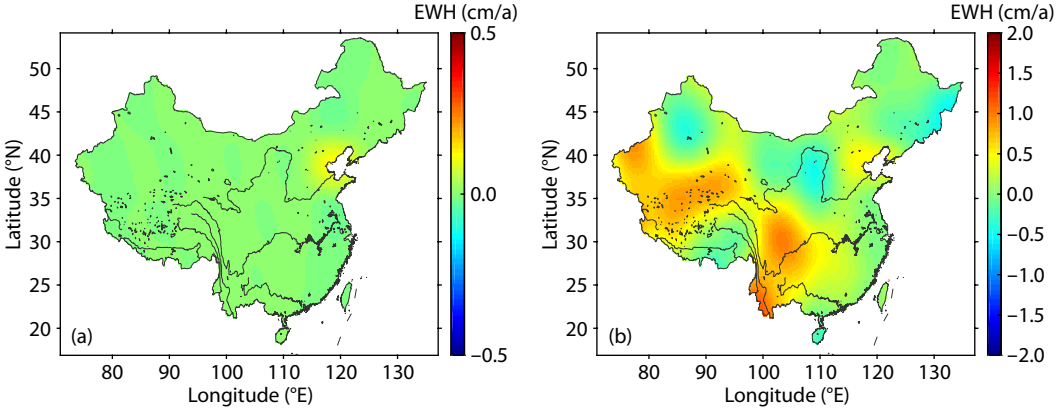

Figure 9. (a) The effect of the time-variable gravity signal caused by sediment mass accumulation in the Bohai Sea on China's coastal areas is obtained by using sediment data collected at the estuary of the Yellow River, (b) time-variable gravity signal after deducting the effect of sediment.

ing the Indian Eurasian plate collision and pointed out that, during the volume transfer, flux from the Indian plate to Eurasia was approximately 4.4 km³/a, including 1.7 km³/a that was denuded; the remaining 2.7 km³/a contributed to the uplift of the Tibetan Plateau and the change in the Moho surface. Of these mass migrations, 9% were transported by rivers along the Himalayas into the Indian Ocean, 11% were brought to the north of the Tibetan Plateau, 23% of the crustal volume flux migrated to the eastern part of the Tibetan Plateau, 43% led to crustal thickening in the Tibetan Plateau, and the remaining 14% impacted equilibrium expansion. The Tibetan Plateau covers an area of approximately 2.5 million square kilometers, of which the positive signal area in the north of the Tibetan Plateau is approximately 1.1 million square kilometers. The eastern region covers an area of approximately 680,000 square kilometers. Therefore, the effect of crustal thickening on the Tibetan Plateau was observed. The equivalent water height was approximately 0.2 cm/a, the effect of volume flux migration on the north was approximately 0.15 cm/a, and the effect on the east was approximately 0.4 cm/a. After modeling, truncating, and filtering these mass transfer signals, the spatial distribution due to the material exchange between India and Eurasia in the north and east of the Tibetan Plateau was obtained, as shown in Figure 10a. For comparison, the contribution of the mass migration of the Tibetan Plateau was subtracted from the residual signal in Figure 9b, giving the spatial distribution map of the residual signal after considering the mass migration signal of tectonic movement, as shown in Figure 10b.

Considering that the uncertainty of the combined hydrological model was ±0.22 cm/a, the signal of time-variable gravity between ±0.22 cm/a in Figure 10b was deducted to obtain the final residual signal distribution, as shown in Figure 10c. There were still some differences between the combined hydrological and tectonic model constructed in this study and the GRACE time-variable gravity field in the north and east of the Tibetan Plateau, yet this difference was very small, indicating that the new combined hydrological and tectonic model of this study is reasonable. The physical sources and mechanisms of the final residual need to be further studied and discussed.

5. Discussion and Conclusions

The purpose of this study was to refine estimates of nonhydrological mass transfer in China continent. The basic idea was to assume that the GRACE time-variable gravity field is composed of surface hydrological mass migration and solid mass migration. If the hydrological signal can be effectively removed from the combined signal, the signal of nonhydrological mass migration can be obtained. For this purpose, the spatial distribution of time-variable gravity signals in China continent was obtained from GRACE gravity satellite observations made between January 2003 and December 2016. Then, from the current hydrological model and other auxiliary hydrological data, a combined hydrological model of China continent was constructed. Finally, the time-variable gravity field corresponding to the combined hydrological model was subtracted from the time-variable gravity field derived from GRACE data, allowing us to obtain a preliminary time-variable gravity field of China's continent nonhydrological mass transfer. The physical sources and mechanisms of this mass transfer were then discussed.

The most critical step in this study was to build a reasonable hydrological model. However, due to the limited water content of the current hydrological model, that model could not represent all hydrological mass changes; differences in accuracy between different versions of the current model also needed to be considered. Therefore, the composition and spatial distribution characteristics of the current hydrological model were analyzed in detail, the hydrological components with the best correlation were selected through correlation calculation, were then analyzed and compared, and a more reasonable combined hydrological model was constructed. This combined hydrological model includes soil water, snow water, vegetation canopy water, groundwater, water in lakes and glaciers, and other water components (mainly reservoir storage, swamps, rivers, etc.) — almost all components of changes in land water reserves.

Using the combined hydrological model developed in this study, the spatial distribution of nonhydrological mass transfer signals in China continent was obtained from the GRACE time-variable total gravity field. The results show that the nonhydrological signals in China continent are mainly positive signals and are distributed in

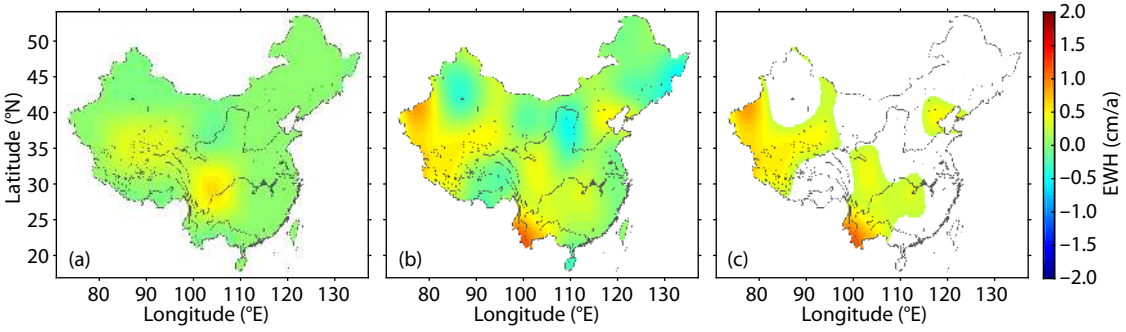

Figure 10. (a) Spatial distribution of time-variable gravity signals due to mass migration over the northern and eastern Tibetan Plateau based on crustal volume equilibrium theory, (b) the time-variable gravity signal after deducting the influence of mass migration caused by tectonic signals in the Tibetan Plateau region and (c) the spatial distribution of residual signal after deducting the nonhydrological signal within the uncertainty range.

the Bohai Rim, and the northern and eastern Tibetan Plateau.

The nonhydrological mass transfer signals obtained as described above were studied and discussed. For the Bohai Rim region, the effects of sea level change and marine sedimentation were considered. Since the influence of sea level change on time-variable gravity information was not included in the hydrological model, ocean altimetry observation data were used to calculate and correct the sea level change. The results show that sea level change effectively weakens the raw residual positive mass migration signal around the Bohai Sea. With regard to the effect of marine sedimentation in the Bohai Sea, the annual sediment transport obtained by the Lijin hydrological control station at the end of the main stream of the Yellow River, from 2003 to 2016, was obtained and used to calculate the impact of sediments on the residual time-variable gravity signal. The result was that the residual nonhydrological mass transfer signal was further weakened. In summary, we conclude that the residual "nonhydrological" mass transfer signal in the Bohai Rim region, within the error range, comes in fact primarily from sea level change and marine sediment accumulation.

The other two positive mass migration signals were distributed in the north and east of the Tibetan Plateau. For this part of our analysis, we used the sedimentological research results of Westaway (1995) from a new perspective to calculate and analyze the net inflow of mass to the Tibetan Plateau; our results indicate that the Tibetan Plateau has a net inflow of 2.7 km³ per million years due to the Indian Eurasian plate collision. This mass inflow contributes to the crustal thickening of the Tibetan Plateau, increasing its mass and leading naturally to an increase in its gravity field. According to this idea, the net mass inflow is converted into a positive change in the gravity field, explaining the increase detected in our modeling, which suggests that the research results presented here are reasonable.

As shown in Figure 10c, there are still some unexplained residuals in the Tibetan Plateau, indicating that some uncertainty remains in the current hydrological model or in solid medium model. The maximum residual in Figure 10c was mainly distributed at the border of China, such as in the Pamir Plateau in the northwest corner and at the border edge of Western Yunnan. The annual and seasonal variations in ice and snow on the Pamir Plateau are large, and the weathering and denudation of high mountains are serious. Currently, there are no reliable denudation observation data or models that would allow accurate calculation of the solid mass transfer in this area. Western Yunnan is affected primarily by the Indian monsoon. Simultaneously, the region has experienced very drastic changes in hydrological mass. There are still some uncertainties in the current observational data and hydrological model. These uncertainties are the possible causes of the residual gravity field in Figure 10c. These problems need to be studied further and discussed.

Acknowledgments

This paper was supported by the National Natural Science Foundation of China (41974093, 41774088, 42174097), the Frontier Science of Chinese Academy of Sciences (qyzdy-sswsys003), China Postdoctoral Science Foundation (2020T130641 and 2020M670424) and Fundamental Research Funds for the Central Universities.

References

Alcamo, J., Döll, P., Henrichs, T., Kaspar, F., Lehner, B., Rösch, T., and Siebert, S. (2003). Development and testing of the WaterGAP 2 global model of water use and availability. *Hydrol. Sci. J.*, *48*(3), 317–337. https://doi.org/10.1623/hysj.48.3.317.45290

Beaudoing, H. , and Rodell, M. (2016). *GLDAS Noah Land Surface Model L4 3 Hourly 0. 25× 0. 25 Degree V2. 1*. Greenbelt: Goddard Earth Sciences Data and Information Services Center (GES DISC).

Bettadpur, S. (2012). *UTCSR Level-2 Processing Standards Document*. Austin: University of Texas.

Chang, L., Tang, H., Wang, Q. Y., and Sun, W. K. (2019). Global thermosteric sea level change contributed by the deep ocean below 2000 m estimated by Argo and CTD data. *Earth Planet. Sci. Lett.*, *524*, 115727. https://doi.org/10.1016/j.epsl.2019.115727

Chang, L., and Sun, W. K. (2020). Greening trends of Southern China confirmed by GRACE. *Remote Sens.*, *12*(2), 328. https://doi.org/10.3390/rs12020328

Chang, L., and Sun, W. K. (2021). Progress and prospect of sea level changes of global and China nearby seas. *Rev. Geophys. Planet. Phys.*, *52*(3), 266–279. https://doi.org/10.19975/j.dqyxx.2020-028

Chen, J. L., Wilson, C. R., and Tapley, B. D. (2010). The 2009 exceptional Amazon flood and interannual terrestrial water storage change observed by GRACE. *Water Resour. Res.*, *46*(12), W12526. https://doi.org/10.1029/2010wr009383

Chen, J. L. (2019). Satellite gravimetry and mass transport in the earth system. *Geod. Geodyn.*, *10*(5), 402–415. https://doi.org/10.1016/j.geog.2018.07.001

Cheng, M. K., and Tapley, B. D. (2004). Variations in the earth's oblateness during the past 28 years. *J. Geophys. Res. Solid Earth*, *109*(B9), B09402. https://doi.org/10.1029/2004jb003028

Döll, P., Kaspar, F., and Lehner, B. (2003). A global hydrological model for deriving water availability indicators: model tuning and validation. *J. Hydrol.*, *270*(1-2), 105–134. https://doi.org/10.1016/s0022-1694(02)00283-4

Dong, J., Cambiotti, G., Wen, H. J., Sabadini, R. and Sun, W. K. (2021). Treatment of discontinuities inside Earth models: Effects on computed coseismic deformations. *Earth Planet. Phys.*, *5*(1), 90–104.

Duong, V. H., Lindenbergh, R., Pfeifer, N., and Vosselman, G. (2008). Single and two epoch analysis of ICESat full waveform data over forested areas. *Int. J. Remote Sens.*, *29*(5), 1453–1473. https://doi.org/10.1080/01431160701736372

Feng, W., Zhong, M., Lemoine, J. M., Biancale, R., Hsu, H. T., and Xia, J. (2013). Evaluation of groundwater depletion in North China using the gravity recovery and climate experiment (GRACE) data and ground-based measurements. *Water Resour. Res.*, *49*(4), 2110–2118. https://doi.org/10.1002/wrcr.20192

Gardner, A. S. , Moholdt, G. , Cogley, J. G. , Wouters, B. , Arendt, A. A. , Wahr, J. , Berthier, E. , Hock, R. , Pfeffer, W. T. , … Paul, F. (2013). A reconciled estimate of glacier contributions to sea level rise: 2003 to 2009. *Science*, *340*(6134), 852–857. https://doi.org/10.1126/science.1234532

Geruo, A., Wahr, J., and Zhong, S. J. (2013). Computations of the viscoelastic response of a 3-D compressible Earth to surface loading: an application to glacial isostatic adjustment in Antarctica and Canada. *Geophys. J. Int.*, *192*(2), 557–572. https://doi.org/10.1093/gji/ggs030

Jacob, T., Wahr, J., Pfeffer, W. T., and Swenson, S. (2012). Recent contributions of glaciers and ice caps to sea level rise. *Nature*, *482*(7386), 514–518. https://doi.org/10.1038/nature10847

Jiao, J. S., Zhang, Y. Z., Yin, P., Zhang, K. N., Wang, Y. P., and Bilker-Koivula, M. (2019). Changing Moho beneath the Tibetan Plateau revealed by GRACE observations. *J. Geophys. Res.: Solid Earth*, *124*(6), 5907–5923. https://doi.org/10.1029/2018jb016334

Koster, R. D. , and Suarez, M. J. (1996). *Energy and Water Balance Calculations in the Mosaic LSM*. Greenbelt: National Aeronautics and Space Administration.

Koster, R. D., Suarez, M. J., Ducharne, A., Stieglitz, M., and Kumar, P. (2000). A catchment-based approach to modeling land surface processes in a general circulation model: 1. Model structure. *J. Geophys. Res. Atmos.*,

105(D20), 24809–24822. https://doi.org/10.1029/2000jd900327

Liang, X., Lettenmaier, D. P., Wood, E. F., and Burges, S. J. (1994). A simple hydrologically based model of land surface water and energy fluxes for general circulation models. *J. Geophys. Res. Atmos.*, *99*(D7), 14415–14428. https://doi.org/10.1029/94jd00483

Matsuo, K., and Heki, K. (2010). Time-variable ice loss in Asian high mountains from satellite gravimetry. *Earth Planet. Sci. Lett.*, *290*(1-2), 30–36. https://doi.org/10.1016/j.epsl.2009.11.053

Moghim, S. (2020). Assessment of water storage changes using GRACE and GLDAS. *Water Resour. Manag.*, *34*(2), 685–697. https://doi.org/10.1007/s11269-019-02468-5

Mu, D. P., Xu, T. H., and Xu, G. C. (2020). An investigation of mass changes in the Bohai sea observed by GRACE. *J. Geod.*, *94*(9), 79. https://doi.org/10.1007/s00190-020-01408-1

Rao, W. L., and Sun, W. K. (2021). Moho interface changes beneath the Tibetan Plateau based on GRACE data. *J. Geophys. Res. Solid Earth*, *126*(2), e2020JB020605. https://doi.org/10.1029/2020jb020605

Rodell, M., Houser, P. R., Jambor, U., Gottschalck, J., Mitchell, K., Meng, C. J., Arsenault, K., Cosgrove, B., Radakovich, J., … Toll, D. (2004). The global land data assimilation system. *Bull. Amer. Meteor. Soc.*, *85*(3), 381–394. https://doi.org/10.1175/bams-85-3-381

Rodell, M., Velicogna, I., and Famiglietti, J. S. (2009). Satellite-based estimates of groundwater depletion in India. *Nature*, *460*(7258), 999–1002. https://doi.org/10.1038/nature08238

Sheng, Y. Y., You, W., Fan, D. M., and Gao, S. T. (2020). Impact of glacial isostatic adjustment models on global mass changes. *J. Geod. Geodyn.*, *40*(11), 1133–1138. https://doi.org/10.14075/j.jgg.2020.11.007

Swenson, S., and Wahr, J. (2006). Post-processing removal of correlated errors in GRACE data. *Geophys. Res. Lett.*, *33*(8), L08402. https://doi.org/10.1029/2005gl025285

Syed, T. H., Famiglietti, J. S., Rodell, M., Chen, J. L., and Wilson, C. R. (2008). Analysis of terrestrial water storage changes from GRACE and GLDAS. *Water Resour. Res.*, *44*(2), W02433. https://doi.org/10.1029/2006wr005779

Tapley, B. D., Bettadpur, S., Watkins, M., and Reigber, C. (2004). The gravity recovery and climate experiment: mission overview and early results. *Geophys. Res. Lett.*, *31*(9), L09607. https://doi.org/10.1029/2004gl019920

Tiwari, V. M., Wahr, J., and Swenson, S. (2009). Dwindling groundwater resources in Northern India, from satellite gravity observations. *Geophys. Res. Lett.*, *36*(18), L18401. https://doi.org/10.1029/2009gl039401

Wahr, J., Molenaar, M., and Bryan, F. (1998). Time variability of the earth's gravity field: hydrological and oceanic effects and their possible detection using GRACE. *J. Geophys. Res. Solid Earth*, *103*(B12), 30205–30229. https://doi.org/10.1029/98jb02844

Wang, Q. Y., Yi, S., and Sun, W. K. (2021). Continuous estimates of glacier mass balance in high mountain Asia based on ICESat-1, 2 and GRACE/GRACE follow-on data. *Geophys. Res. Lett.*, *48*(2), e2020GL090954. https://doi.org/10.1029/2020gl090954

Westaway, R. (1995). Crustal volume balance during the India-Eurasia collision and altitude of the Tibetan Plateau: a working hypothesis. *J. Geophys. Res. Solid Earth*, *100*(B8), 15173–15192. https://doi.org/10.1029/95jb01310

Xing, L. L., Liu, Z. W., Jia, J. G., Wu, S. Q., Chen, Z. S. and Niu, X. W. (2021). Far-field coseismic gravity changes related to the 2015 M_W7.8 Nepal (Gorkha) earthquake observed by superconducting gravimeters in Chinese mainland. *Earth Planet. Phys.*, *5*(2), 141–148. https://doi.org/10.26464/epp2021018

Yi, S., and Sun, W. K. (2014). Evaluation of glacier changes in high-mountain Asia based on 10year GRACE RL05 models. *J. Geophys. Res.: Solid Earth*, *119*(3), 2504–2517. https://doi.org/10.1002/2013jb010860

Yi, S., Freymueller, J. T., and Sun, W. K. (2016a). How fast is the middle-lower crust flowing in eastern Tibet. *A constraint from geodetic observations. J. Geophys. Res.: Solid Earth*, *121*(9), 6903–6915. https://doi.org/10.1002/2016jb013151

Yi, S., Wang, Q. Y., Chang, L., and Sun, W. K. (2016b). Changes in mountain glaciers, lake levels, and snow coverage in the Tianshan monitored by GRACE, ICESat, altimetry, and MODIS. *Remote Sens.*, *8*(10), 798. https://doi.org/10.3390/rs8100798

Zhang, G. Q., Yao, T. D., Xie, H. J., Kang, S. C., and Lei, Y. B. (2013). Increased mass over the Tibetan Plateau: from lakes or glaciers. *Geophys. Res. Lett.*, *40*(10), 2125–2130. https://doi.org/10.1002/grl.50462

Zhang, G. Q., Chen, W. F., and Xie, H. J. (2019). Tibetan Plateau's lake level and volume changes from NASA's ICESat/ICESat-2 and Landsat missions. *Geophys. Res. Lett.*, *46*(22), 13107–13118. https://doi.org/10.1029/2019GL085032

Zhang, L., Yi, S., Wang, Q. Y., Chang, L., Tang, H., and Sun, W. K. (2019). Evaluation of GRACE mascon solutions for small spatial scales and localized mass sources. *Geophys. J. Int.*, *218*(2), 1307–1321. https://doi.org/10.1093/gji/ggz198

Zhang, L., and Sun, W. K. (2022). Progress and prospect of GRACE Mascon product and its application. *Reviews of Geophysics and Planetary Physics*, *53*(1): 35–52. (in Chinese). https://doi.org/10.19975/j.dqyxx.2021-033